Journal of Non-Newtonian Fluid Mechanics 304 (2022) 104806

Contents lists available at ScienceDirect

Journal of Non-Newtonian Fluid Mechanics

journal homepage: www.elsevier.com/locate/jnnfm

3D simulation of the hierarchical multi-mode molecular stress function constitutive model in an abrupt contraction flow

P. Olley [a,*], T. Gough [a], R. Spares [b], P.D. Coates [a]

[a] Faculty of Engineering & Informatics, University of Bradford, United Kingdom
[b] Now at Covvi, Leeds, United Kingdom

ARTICLE INFO

Keywords:
Molecular stress function
Hierarchical multi-mode molecular stress function
HMMSF
Simulation
Abrupt contraction
Vortex
Birefringence
Stress optical coefficient

ABSTRACT

A recent development of the Molecular Stress Function constitutive model, the Hierarchical Multi-Mode Molecular Stress Function (HMMSF) model has been shown to fit a large range of rheometrical data with accuracy, for a large range of polymer melts. We develop a 3D simulation of the HMMSF model and compare it to experimental data for the flow of Lupolen 1840H LDPE through an abrupt 3D contraction flow. We believe this to be the first finite element implementation of the HMMSF model. It is shown that the model gives a striking agreement with experimental vortex opening angles, with very good agreement to full-field birefringence measurements, over a wide range of flow rates. A method to give fully-developed inlet boundary conditions is implemented (in place of using parabolic inlet boundary conditions), which gives a significantly improved match to birefringence measurements in the inlet area, and in low stress areas downstream from the inlet. Alternative constitutive model parameters are assessed following the principle that extensional rheometer data actually provides a 'lower bound' for peak extensional viscosity. It is shown that the model robustly maintains an accurate fit to vortex opening angle and full-field birefringence data, provided that both adjustable parameters are kept such that both shear and extensional data are well fitted.

1. Introduction and background

The simulation and modelling of viscoelastic melt flows has advanced considerably with the introduction of molecularly based constitutive models. Earlier models such as the separable KBKZ [1] typically gave an accurate response in shear and uniaxial extension, and a qualitatively correct response to vortex growth in simulations of axisymmetrical abrupt contraction flows. However, this class of model typically gave a much less accurate response in planar and equibiaxial extension, and also showed a much reduced predictive capability for vortex opening angle in simulations of abrupt planar contractions (see eg[2].). Explicit molecular considerations were brought into constitutive models with models such as the Molecular Stress Function model [3,4], the Pom-Pom model [5,6], and the introduction of the Convective Constraint Release (CCR) mechanism [7]. The Molecular Stress Function (MSF) model uses an energy balance approach to predict viscoelastic stresses for a given deformation history, and has been shown to fit a wide range of viscometric measurements for long chain branched and linear polymers [3,4,8] whilst using only two adjustable parameters. A version with a CCR mechanism, the MSF-CCR [4] has also been shown to give a good qualitative agreement in 3D simulation, in comparison to measured vortex opening angles for an abrupt contraction flow, and near-quantitative agreement with full-field stress birefringence measurements [9].

Many other comparisons have been made between experimental data and simulations of other constitutive models that give a realistic response in planar extensional flow. Such models include the eXtended Pom-Pom (XPP) [10,11], the Double Convected Pom (DHPP) [12], and the tube based CCR model of Marrucci & Iannirubertо [13,14]. For these models, vortex opening angles were compared with experiment in ref [10], full field birefringence was compared in refs [11,13] along with laser doppler anemometry, and centreline measurements of birefringence and velocity were compared in ref [12]. The experimental data reported in detail in ref [9] provides a particularly demanding test for a constitutive model in complex flow since it allows the comparison of two quantities that are particularly sensitive to material properties, namely vortex opening angles and birefringence, and the data are given across a large range of flow rates.

A recent development of the MSF model, the Hierarchical Multi-Mode Molecular Stress Function model (HMMSF) incorporates a

* Corresponding author.
E-mail address: p.olley@bradford.ac.uk (P. Olley).

https://doi.org/10.1016/j.jnnfm.2022.104806
Received 11 January 2022; Received in revised form 5 April 2022; Accepted 7 April 2022
Available online 9 April 2022
0377-0257/© 2022 The Author(s). Published by Elsevier B.V. This is an open access article under the CC BY license (http://creativecommons.org/licenses/by/4.0/).

dynamic dilution mechanism [15,16] related to the relaxation rates of the polymer segments. This model has been shown to give good agreement (for both long chain branched and linear polymers) to a wide range of viscometric rheological measurements made in shear flow, and in uniaxial, planar and equibiaxial extension [16,17,18]. The model again uses only two freely adjustable parameters, and has also been shown to give rheological predictions that are largely independent of the number of relaxation modes employed [15]. Ref [19] compares many constitutive models of current interest and shows that avoiding using a pre-averaged stretch formulation in a model is crucial to the model being able to achieve a good fit to rheometric data with very few (2 or 3) adjustable parameters.

We apply the HMMSF model to the simulation of the same 3D abrupt contraction flow of a LDPE melt described in ref [9], and show it gives strikingly good agreement with experimental vortex opening angles for this flow, with very good agreement to birefringence measurements.

2. The HMMSF model and parameter estimation

The Hierarchical Multi-Mode Molecular Stress Function (HMMSF) model takes the form:

$$\boldsymbol{\tau}(t) = \int_{-\infty}^{t} m(t,t^{'})\, f_i^2(t,\ t^{'})\ \boldsymbol{S}_{\mathbf{DE}}^{\mathbf{IA}}(t,t^{'})\ \mathrm{d}t^{'} \tag{1}$$

where $\boldsymbol{\tau}(t)$ is the stress at the current time, t, and t' is any time in the past. $\boldsymbol{S}_{\mathbf{DE}}^{\mathbf{IA}}(t,t^{'})$ is the Doi-Edwards stress tensor, using the independent alignment (IA) assumption, given by

$$\boldsymbol{S}_{\mathbf{DE}}^{\mathbf{IA}}(t,\ t^{'}) = 5\left\langle \frac{u^{'}\ u^{'}}{u^{'2}} \right\rangle, \tag{2}$$

where u' is the length of a deformed unit vector u', and $\langle \ldots \rangle$ denotes a spherical average [16]. $m(t,t')$ is the memory function between t' and t, and $f_i(t,t')$ is the Molecular Stress Function associated with relaxation mode i [16]. The memory function is commonly represented by a spectrum of relaxation times, τ_i, and relaxation moduli, g_i, using

$$m(t,t') = \sum_i \frac{g_i}{\tau_i} e^{-(t-t')/\tau_i} \tag{3}$$

The HMMSF model contains a hierarchical concept whereby the shortest relaxation times associated with a polymer have a dilution effect upon the longer relaxation times. This is contained within the evolution equation of the Molecular Stress Function:

$$\frac{\partial f_i}{\partial t} = f_i(\boldsymbol{k}:\boldsymbol{S}) - \frac{1}{\alpha}\left(\frac{1}{\tau_i} + \beta CR\right)\left[(f_i - 1)\left(1 - \frac{2}{3}w_i^2\right) + \frac{2}{9}f_i^2\left(f_i^3 - 1\right)w_i^2\right].. \tag{4}$$

In the evolution equation, $\mathbf{k}$ is the velocity gradient tensor (given by $k_{ij} = \frac{\partial u_i}{\partial x_j}$), $\mathbf{S}$ is the orientation tensor, and CR is the constraint release mechanism. The parameter α has the fixed value of 1 for long chain branched (LCB) polymers, or the value of 1/3 for linear polymers. The constraint release parameter, β, is adjustable. w_i in eq. (4) represents the mass fraction of dynamically diluted polymer segments associated with a relaxation mode, i. It is calculated from:

$$w_i^2 = \frac{1}{G_D}\sum_{j=1}^{n} g_j\, e^{-\tau_i/\tau_j} \mathrm{for} \tau_i > \tau_D, \tag{5}$$

or

$$w_i^2 = 1 \mathrm{for} \tau_i \le \tau_D \tag{6}$$

where τ_D is the time for the overall relaxation modulus of the polymer to relax to the value of the parameter G_D. For computational purposes this means that w_i^2 (for each mode i) can be calculated from eq. (5), but must then be capped to value 1 if it exceeds that value.

Table 1
Relaxation spectrum obtained for Lupolen 1840H at 150 °C.

i	λ_i (s)	g_i (Pa)
1	1.000E-03	1.187E+05
2	6.060E-03	6.340E+04
3	3.672E-02	3.237E+04
4	2.225E-01	1.663E+04
5	1.348E+00	6.968E+03
6	8.170E+00	2.266E+03
7	4.951E+01	4.147E+02
8	3.000E+02	2.414E+01

The constraint release mechanism, CR, is given by

$$CR = \frac{1}{2}\sqrt{\left|\mathbf{A}_2 : \mathbf{S} - \ \mathbf{A}_1^2 : \mathbf{S}\right|}. \tag{7}$$

$\mathbf{A}_1$ and $\mathbf{A}_2$ are the first and second Rivlin-Erickson tensors, given by:

$$\mathbf{A}_1{}^2 = 4\mathbf{D}^2, \tag{8}$$

and

$$\mathbf{A}_2 = \frac{\mathrm{D}\mathbf{A}_1}{\mathrm{Dt}} + \mathbf{A}_1{}^2 + 2\left(\mathbf{W}\cdot\mathbf{D} + \mathbf{D}\cdot\mathbf{W}^{\mathbf{T}}\right), \tag{9}$$

where $\mathbf{W}$ and $\mathbf{D}$ are the rate of rotation tensor, and the rate of deformation tensor respectively, given by $\mathbf{W} = \frac{(\mathbf{k}-\mathbf{k}^{\mathbf{T}})}{2}$ and $\mathbf{D} = \frac{(\mathbf{k}+\mathbf{k}^{\mathbf{T}})}{2}$.

Full details of the underlying theory are given in reference [16].

The model has only two freely adjustable parameters, the dilution modulus, G_D, and the constraint release parameter, β. G_D sets the time, τ_D, at which dynamic dilution takes effect [16], and the dynamic dilution of relaxation mode i is the larger the longer the relaxation time τ_i. The overall effect of this on constant rate elongational simulation is to moderate the plateau stress value, and also to modify the stress growth rate. The stress in constant shear simulation is also moderated by this parameter. The constraint release parameter, β, weights the effect of the constraint release term, CR. In shear flow the term further limits the stress growth, however in purely extensional flows the parameter has no effect since the term $\mathbf{A}_2 : \mathbf{S} - \ \mathbf{A}_1^2 : \mathbf{S}$ is then zero.

The relaxation spectrum for the memory function for Lupolen 1840H was obtained from measurement of the storage and loss moduli (G' and G'') of the material using a 25 mm parallel plate geometry mounted on an Anton Paar MCR501 rheometer at 150 °C. Particular attention was paid to obtaining results at as low a rate as possible (0.01 rads/s was obtained) in order to allow long relaxation times to be included in the derived spectrum. The method given in [20] was then used to derive the relaxation spectrum, using 8 relaxation times between $1 \times 10^{-3}s$ and $3 \times 10^{2}s$, as given in Table 1.

Reference [20] makes the point that beyond a certain number of modes, $\widetilde{N}$, there is little discernible improvement in the least-squares error between the measured data points, and predictions from the relaxation spectrum; essentially the extra modes are being used to fit noise beyond this number. This number $\widetilde{N}$ can be identified by plotting the least-squares error against the number of modes used, to see where the error stops reducing significantly [20]. For our data, least-squares error was calculated between 3 and 13 modes and found to stop reducing significantly beyond 10 modes, hence the use of 8 modes is not excessive for this data. The values of G' and G'' predicted by the resulting spectrum are compared with the original measurement data in Fig. 1, and show excellent agreement.

To obtain fitting parameters for the HMMSF model for Lupolen 1840H we first consider the published uniaxial elongational data of Sentmanat et al. at 150 °C [21]. Fig. 2 shows the published data; it was reported in that paper that "necking" was clearly seen during the tests at points corresponding to drops in the stress, using video techniques. The same figure shows the predictions of the HMMSF model using a value of

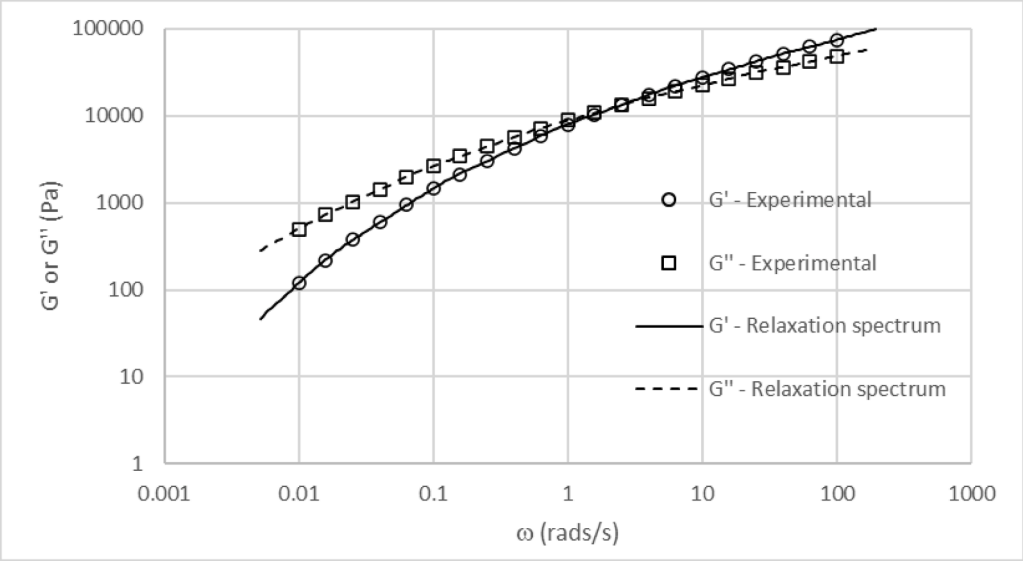

Fig. 1. G' and G'' measured at 150 °C, compared with predictions from the derived relaxation spectrum.

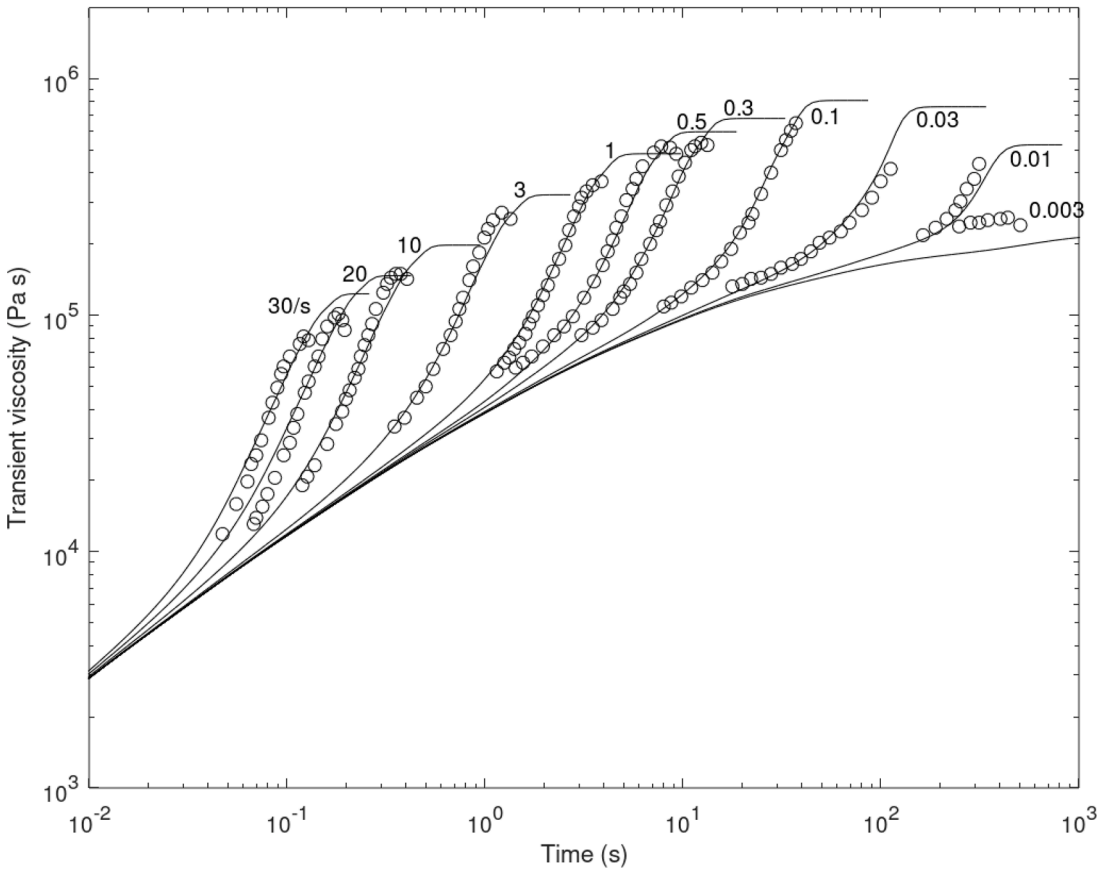

Fig. 2. Comparison of the uniaxial elongational measurements of Lupolen 1840H at 150 C (from [21]) and the HMMSF model with $G_D = 7 \times 10^3\ Pa$.

$G_D = 7 \times 10^3\ Pa$.

The fit to the elongational data is exceptionally good in terms of growth rate, over a large range of elongational rates. The value of $G_D = 7 \times 10^3\ Pa$ is consistent with taking the experimental data as being a "lower bound" of stress [16], as the simulated curves are generally on, or just rise closely above, the experimental data. The underprediction of strain hardening at the very lowest rates is not surprising since the longest time constant used in simulation is 300 s (a limit imposed by the minimum rotation rate that could be measured using the rotational rheometer), and so the ability to predict strain hardening reduces at rates around the inverse of this, giving slight underprediction of strain hardening at $0.01s^{-1}$ and strong underprediction at $0.003s^{-1}$.

Shear viscosity data is required to establish a value for the parameter, β. Zatloukal gives steady-state shear viscosity data for Lupolen 1840H at 180 °C, obtained using a capillary rheometer [22]. This data was time-temperature shifted to 150 °C as described in [9] for comparison

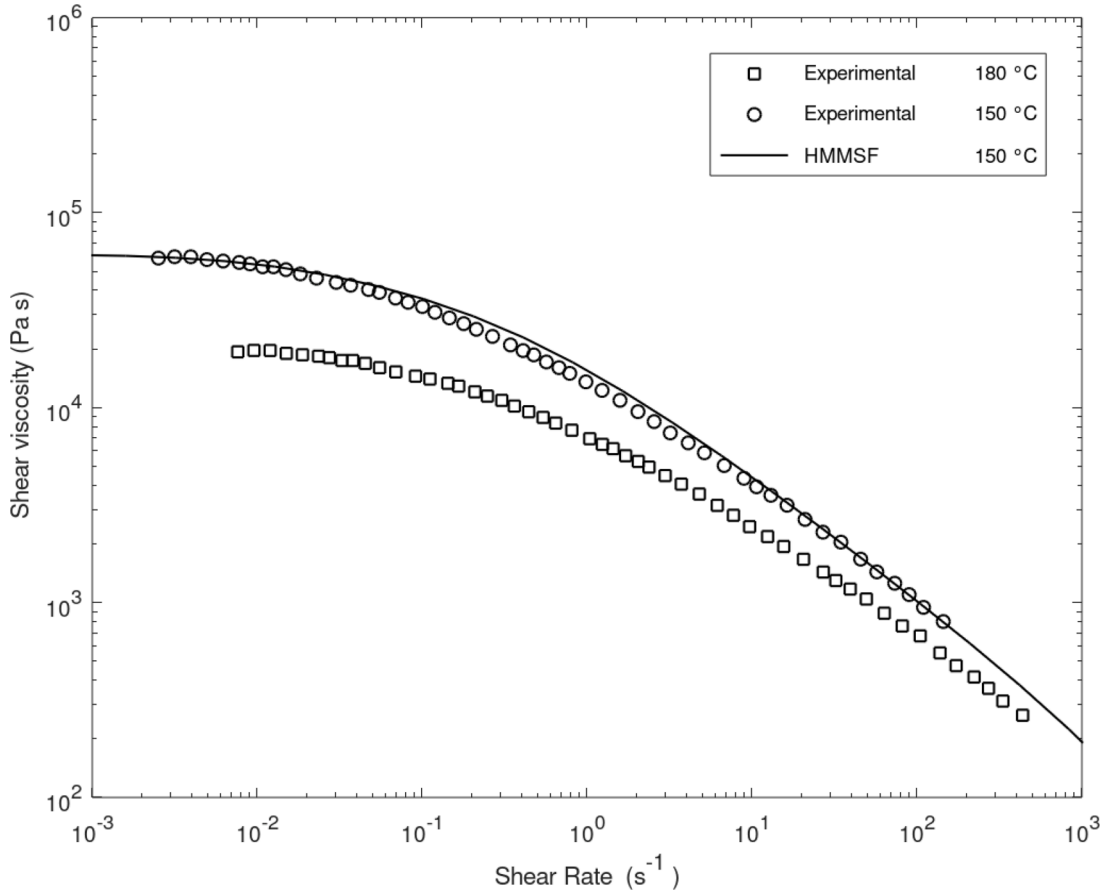

Fig. 3. Shear viscosity measurements of Lupolen 1840H (from [22]) and the same data after time-temperature shifting to 150°*C*, compared with predictions from the HMMSF model using $G_D = 7 \times 10^3\ Pa$ and $\beta = 0.04$.

with the HMMSF predictions at that temperature. Fig. 3 shows the original 180 °C data, the experimental data time-temperature shifted to 150 °C, and the simulated steady-state response of the HMMSF model using a value of $G_D = 7 \times 10^3\ Pa$ with $\beta = 0.04$.

The prediction at 150 °C follows the line of the experimental data at 150 °C, albeit with a slight overprediction at the centre rates of the graph. It is worth noting that the HMMSF model has been shown to give a very close predictive agreement with the transient shear viscosity for a large range of LCB and linear polymers (eg [16,17]).

3. 3-D modelling and implementation of the HMMSF model

Details of our simulation of the MSF-CCR model for 2D and axisymmetric flows are given in ref [23], and details of the extension of this implementation to 3D are given in [9]. An outline of this 3D simulation method is given here, along with the new details of implementing the HMMSF model.

3.1. Mesh and tracking

For 3D modelling we used the 27 noded tri-quadratic element giving quadratic interpolation of velocity components, and 8-noded tri-linear elements giving one order less for pressure.

In order to calculate the current stress, $\boldsymbol{\tau}(t)$, according to eq. (1), it is necessary to track a particle backwards in time to any time t' in the past. The Doi-Edwards tensor of eq. (1) can then be calculated from the deformation gradient tensor, $\boldsymbol{F}(t, t')$, which is calculated along the path using:

$$\frac{d\boldsymbol{F}(t,t')}{dt'} = \mathbf{k}(t')\,\mathbf{F}(t,t'), \tag{10}$$

where $\mathbf{k}(t')$ is the velocity gradient tensor evaluated at time t'.

The position of the particle can by progressively tracked back in time by successive applications of the kinematic procedure

$$\begin{aligned} x(t'-\delta t') &= x(t') - u\delta t' + \frac{\delta t'^2}{2}\left(u\frac{\partial u}{\partial x} + v\frac{\partial u}{\partial y} + w\frac{\partial u}{\partial z}\right), \\ y(t'-\delta t') &= y(t') - v\delta t' + \frac{\delta t'^2}{2}\left(u\frac{\partial v}{\partial x} + v\frac{\partial v}{\partial y} + w\frac{\partial v}{\partial z}\right), \\ z(t'-\delta t') &= z(t') - w\delta t' + \frac{\delta t'^2}{2},\left(u\frac{\partial w}{\partial x} + v\frac{\partial w}{\partial y} + w\frac{\partial w}{\partial z}\right), \end{aligned} \tag{11}$$

where *u, v* and *w* are the velocity components in the x, y and z directions respectively, and $\delta t'$ is a small step in historical time. As the tracking proceeds, values of the velocity gradient tensor, $\mathbf{k}$, the deformation gradient tensor, $\mathbf{F}(t,t')$ and the numerical evaluation of $\mathbf{k} : \mathbf{S}$ are stored for later (repeated) use in integrating the Molecular Stress Functions, f_i.

In 3D there is no streamfunction that can be used to correct small errors accumulated by this procedure, however it was shown in [9] that, in a comparison for a LDPE in a 2D abrupt contraction flow - both with and without streamline correction, there was a maximum difference in opening angle of 0.5° and a negligible difference in birefringence patterns over a large range of flow rates. As the primary experimental values being compared in this work are opening angles and birefringence measurements, then the tracking method described is appropriate.

3.2. Computation of the Doi-Edwards tensor and the molecular stress function

Once the deformation gradient tensor, $\boldsymbol{F}(t, t')$ is known, the Doi-Edwards tensor with independent alignment assumption, $\boldsymbol{S}_{\mathbf{DE}}^{\mathbf{IA}}(t,t')$, can be calculated directly. This can be done very efficiently using Currie's approximation [24], and used in calculating stress through eq. 1.

The calculation of $f_i(t,t')$ for eq. (1) is structurally different in that, having stepped *backwards* in time to time t', $f_i(t,t')$ must be calculated by integrating eq. (4) *forwards* in time, starting from a value of $f_i(t,t')=1$ at time t'. There are many similarities to how the MSF-CCR function is integrated in ref [23], but there are two significant differences:

1 the computation must be performed for each mode, i.
2 the factor $\frac{1}{\alpha}\left(\frac{1}{\tau_i}+\beta\, CR\right)$ in eq. (4) can be very large, especially for small relaxation times, and so reduced time integration steps are needed for stability and accuracy. After experimentation with different strategies, limiting the integration time step such that dt' $f_i^2(t,t')/(\alpha\,\tau_i) < 0.1$ proved to be robust and efficient in the simulations covered. Note this is an additional limit, in addition to limits arising from the adaptive 4th order Runga-Kutta used in performing the integration, as described in ref [23].

It is computationally very expensive to calculate $f_i(t,t')$ directly at every value of t' stored for the time-integration of eq. (1). Instead we use an adaptive point selection method, whereby an initial selection of points have $f_i(t,t')$ calculated directly; it is then checked if the calculated value at each point can be deduced sufficiently accurately by linear interpolation from the two points either side. If so, then linear interpolation can be used within that section, or if not then further points must have their values of $f_i(t,t')$ computed directly, until linear interpolation gives sufficient accuracy. The process continues iteratively until $f_i(t,t')$ can be calculated by interpolation of calculated points over all sections of the history. This adaptive point selection approach gives a very large reduction in the time needed to calculate stress. Full details of the approach are given in ref [23].

Once the Doi-Edwards tensor and corresponding Molecular Stress Function are known for each historical point in time, t', the integration of eq. (1) can be accomplished, and the stress at each required point in the flow can be ascertained.

In our implementation the stress is required at all Gauss points within each element, a total of 27 points per element using "3-point Gauss" in 3D elements.

3.3. Computation of velocity and pressure field

For an assumed steady-state solution, we require the velocity field that produces the stress field given by eq. (1). In addition, for a steady-state solution, the stress field must satisfy Cauchy's equation:

$$\nabla\cdot(\boldsymbol{\tau}-\mathbf{I}p)=0, \tag{12}$$

where p is pressure, and $\mathbf{I}$ is the identity matrix. Using the method of [25], velocity is introduced by subtracting notional Newtonian viscous stresses from each side of the equation. These viscous stresses are given by $\mu\,(\mathbf{k}+\mathbf{k}^{\mathbf{T}})$, where μ is a viscosity that is related to the low-rate shear viscosity of the polymer (see ref [23]), and $\mathbf{k}$ is the velocity gradient tensor. This leads to

$$-\nabla.\left(\mu\left(\mathbf{k}+\mathbf{k}^{\mathrm{T}}\right)-\mathbf{I}p\right)=\nabla.\left(\boldsymbol{\tau}-\mu\left(\mathbf{k}+\mathbf{k}^{\mathbf{T}}\right)\right) \tag{13}$$

The right hand side is a force vector, which can be calculated from the stresses arising from an initial flow estimation (typically a Newtonian solution). The left hand size is a matrix containing pressure and velocity components. Solution of this system of equations gives an updated solution of the velocity components and pressure. The stress values are then recalculated for this new flow field, according to eq. (1), and the procedure is iterated until satisfactory convergence is attained. In this work we obtained a relative convergence of at least 5×10^{-4} for both velocity and pressure over all flow rates.

Table 2
Relationship between mass and volumetric flow rates, and apparent shear rates.

Screw speed (rpm)	5	10	15	25	40
Mass flow rate ($g\ min^{-1}$)	14.4	28.8	43.0	73.3	117.3
$Q\ (m^3\ s^{-1})$	3.08×10^{-7}	6.15×10^{-7}	9.19×10^{-7}	1.57×10^{-6}	2.51×10^{-6}
$\dot{\gamma}_a(s^{-1})$	5.25	10.5	15.7	26.7	42.8

3.4. Computation of stress birefringence patterns

In order to compare simulated stresses with experimental stress birefringence images, the method of Clemeur et al. [12] was used to calculate birefringence patterns that would arise from the simulated stresses. In this method a Mueller matrix is calculated along a line of sight through the polymer. For birefringence seen in the z direction the equation is:

$$\frac{d\boldsymbol{M}(z)}{dz}=\boldsymbol{m}(z)\cdot\boldsymbol{M}(z), \tag{14}$$

where $\boldsymbol{M}(z)$ is the Mueller matrix (initially a 4×4 identity matrix), and $\boldsymbol{m}(z)$ is a matrix built up from stress components that act normally to z; the wavelength of light and the Stress Optical Coefficient, C, are also used in the matrix (see [12] for full details of $\boldsymbol{m}(z)$). The method calculates the cosine of the retardation angle, δ, and birefringence stress pattern can then be produced by plotting the brightness proportional to $1-cos(\delta)$ for comparison to "crossed polarisers" (i.e. where the polarisers used in experimental birefringence are at 90° to one another, which gives a dark fringe at zero stress), or proportional to $1-cos(\delta+\pi)$ for comparison to "uncrossed polarisers, which gives a light fringe at zero stress. Additionally there is likely to be some stress 'history' within the polymer from passing through the extruder; this history is essentially unknown, but must contribute some phase shift in birefringence. We accommodate this by plotting the brightness proportional to $1-cos(\delta+\theta)$, where θ is a phase shift.

4. 3D simulation and comparison with experimental results

The experimental results, reported in detail in ref [9], were made on a 4:1 contraction ratio die with significant 3D effects introduced by a 5:3 upstream width to height ratio. Measurements were made at extruder screw speeds of 5, 10, 15, 25 and 40 rpm. The lower limit was set by instabilities in the flow below 5 rpm (this low speed instability has been reported many times for experimental contraction flows of LDPE, see [26]). The upper limit was set by the strength of the seals of the glass windowed die. Vortex opening angles and stress birefringence images were recorded at each rate.

The mass flow rate of the flow at each screw speed was measured directly by collecting polymer output and gave rates of 14.4 g/min, 28.8 g/min, 43.0 g/min, 73.3 g/min and 117.3 g/min, respectively. The density of Lupolen 1840H at 150 °C has been measured as 780 kg/m^3 [27] which allows the volumetric flow rates, Q, to be determined. From these the apparent shear rate, $\dot{\gamma}_a$, can be calculated using $\dot{\gamma}_a = 6Q/W(2h)^2$, where W is the width of the slit and $2h$ is the height of the slit downstream from the contraction. The corresponding flow rates and apparent shear rates are given in ref [9], and are repeated here for convenience, in Table 2.

Fig. 4 shows the mesh used for the simulations, referred to as Mesh-1.0. Other meshes are used later in this work for a mesh convergence

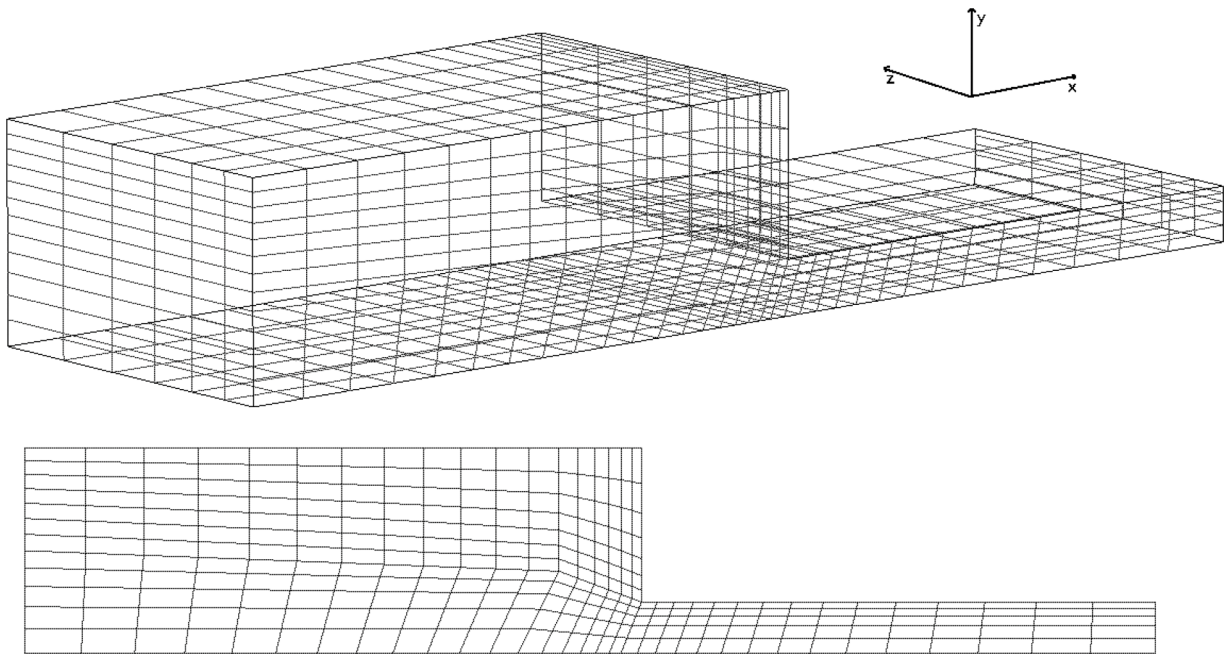

Fig. 4. Surfaces of the 3D Mesh of 27 noded elements using 2 planes of symmetry (top), with section of the mesh in the x-y plane (bottom).

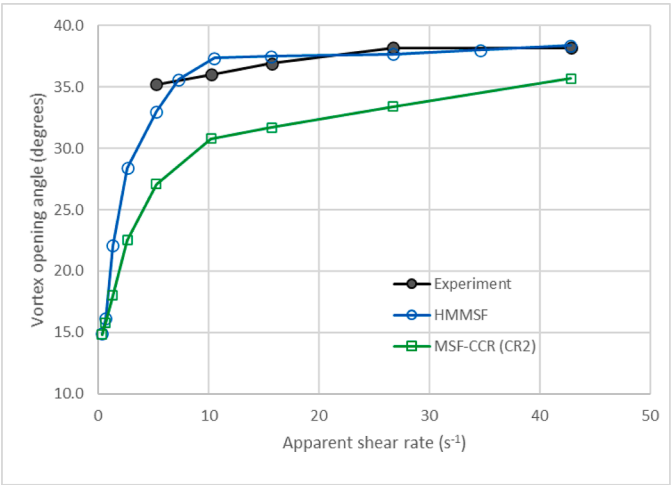

Fig. 5. Comparison between experimental results and simulation results using the HMMSF model (with $G_D = 7 \times 10^3\ Pa$ and $\beta = 0.04$) and the MSF-CCR model (with constraint release mechanism CR2 (see ref [9] for full definition and context), using a_1=0.012 and a_2=0.65). Fully developed inlet boundary conditions were used in both sets of simulations.

study. Symmetry in the y and z planes were used, implemented by zeroing the velocities normal to the planes of symmetry. The mesh employed 1746 27-noded elements, with a total of 16,315 nodes.

Fig. 5 compares opening angle from experiment, and those given by the HMMSF model. For comparison, results using the MSF-CCR are given using the same mesh and same fully-developed boundary conditions (see [9]). The reason for showing the MSF-CCR model results is that these are the best previous simulation results we are aware of against this set of experimental results.

Earlier work on this simulation problem [9] used a parabolic form for the inlet profile. In this work a fully-developed inlet flow is used. The simulation starts with a parabolic form, but then progresses towards fully-developed inlet boundary conditions by "mirroring back", to the inlet, the flow profile a short distance downstream. In this work the flow profile was mirrored back from a line approximately 1.5 elements downstream of the inlet; this distance was used as it is equal to several node separations and the distance allows the inlet flow to evolve significantly towards its fully-developed profile. The total flow rate through the inlet was calculated before and after the inlet boundary condition changes, and the individual boundary condition velocities were corrected by the ratio of these two rates, which prevents any incremental drift of overall volumetric flow rate. The strategy used was to perform this update every 4th iteration, to allow any associated instabilities to settle between changes. The changes to boundary condition values progressively became smaller as the inlet approached the true fully-developed profile. The update procedure was discontinued after 15 applications (by which point the changes were negligible) to give fixed boundary conditions for the remaining convergence iterations.

A fully-developed inlet boundary condition is clearly closer to the true situation than the parabolic boundary conditions used previously (in [9]), and were found to give a notably better match to stress birefringence measurements near the inlet and also in low stress areas downstream from the inlet. Comparisons of simulated birefringence images using fully-developed, and parabolic, inlet boundary conditions are shown in Appendix A. Another effect was found to be that the vortex opening angles were generally one or two degrees lower than with a parabolic inlet profile. This shows that the form of the inlet boundary conditions has a significant effect on opening angles, and the more accurate fully-developed form is to be preferred to approximations such as a 2D parabolic form. The method described above for obtaining the fully developed flow is effective, and relatively easy to implement compared with a method such as initially solving a 2D cross section of the viscoelastic flow.

4.1. Opening angles

Experimentally, vortex opening angles were measured by introducing a small quantity of glass tracer particles into the flow, in conjunction with laser sheet lighting on the centre-plane. The vortex opening angles were then measured from individual frames of video recordings. See ref [9] for details.

The streamfunction, ψ, defined by $\frac{\partial \psi}{\partial y} = u$ and $\frac{\partial \psi}{\partial x} = -v$ is valid in 2-D and axisymmetric flows, but is not generally valid in 3D flows. However as deduced in [9], the streamfunction is valid in the current problem on

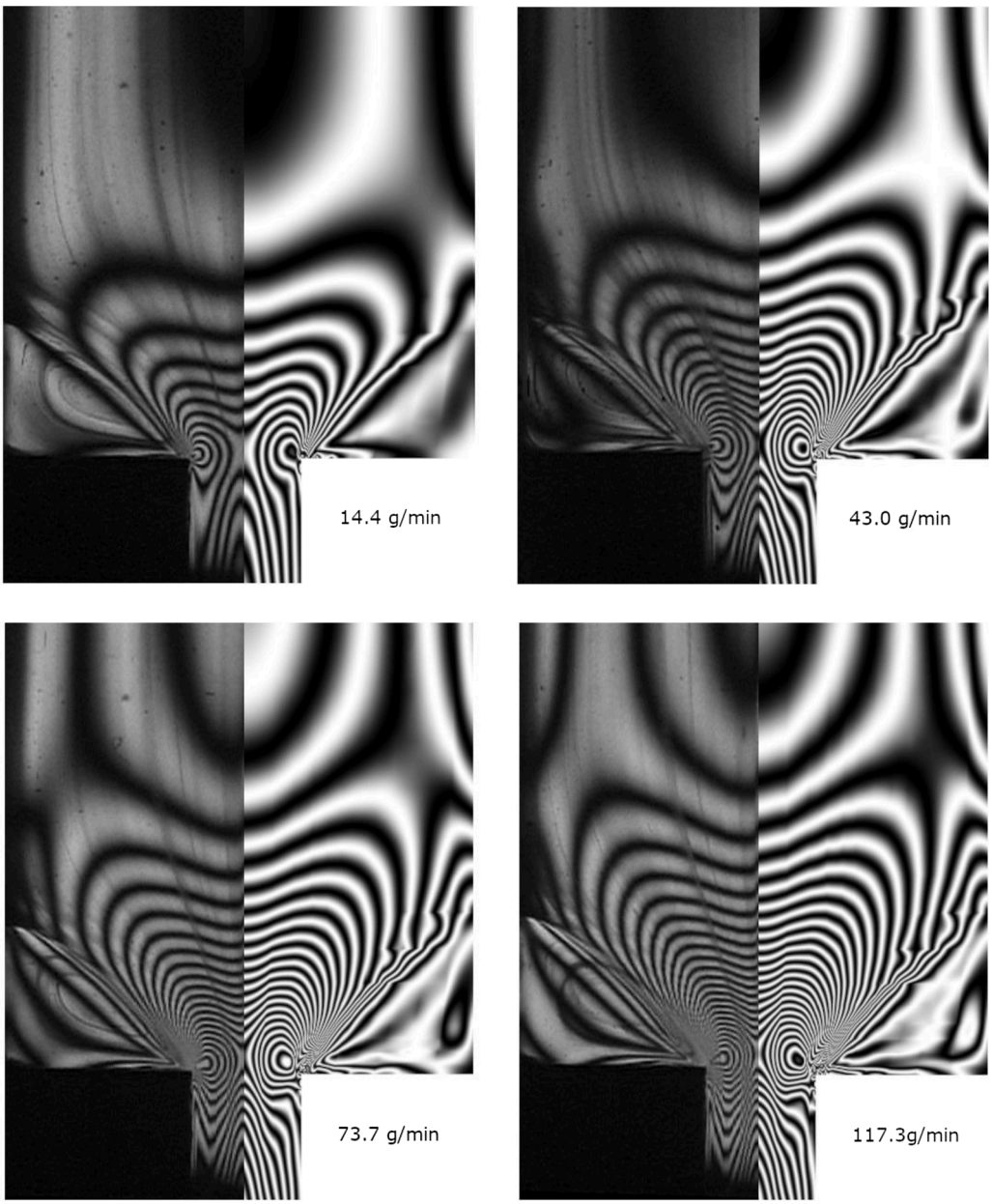

Fig. 6. Comparison between experimental birefringence measurements (left) and computed birefringence resulting from simulation using the HMMSF model (right), for a range of flow rates using $G_D = 7 \times 10^3\ Pa$ and $\beta = 0.04$.

the centreplane (where $z = 0$) only. Hence the streamfunction could be calculated on the symmetry plane $z = 0$, subject to the boundary condition that $\psi = 0$ on the top walls. This streamfunction was used as the primary means of measuring opening angle, with confirmation given by viewing the vectors on the centre-plane, as was illustrated in ref [9] .

The experimental opening angles can be seen to rise from approximately 35° at the lowest flow rate measured to approximately 38° at the highest rate. It is useful to recall that the lowest flow rate was limited by pulsing of the flow, hence no steady angle could be determined for flows below that rate. The HMMSF model matches closely over the full experimental range, with a maximum discrepancy of 2°. It is also apparent that the HMMSF, with these parameters, gives a nearly flat response once a certain level has been reached (a detailed examination shows that the simulated opening angle rises continuously over the range of experiment). It is interesting that below the lowest flow rate at which a steady opening angle was seen experimentally, the HMMSF rises rapidly with flow rate, from Newtonian vortex levels to almost the experimental 'near-plateau' level.

The improvement in accuracy over the best previously known results, the MSF-CCR model, can be seen clearly. Improvement can be seen both quantitatively in the proximity of simulation and experimental values, and qualitatively in the more 'plateau-level' nature of the opening angles at medium and high rates.

4.2. Comparison of birefringence results

As described earlier, birefringence images were reconstructed from the stress components of the simulation results using the method of Clemeur et al. [12]. As was discussed in ref [9], obtaining a reliable value for the Stress Optical Coefficient, C, is notoriously difficult with differences of over 40% being reported between different measurement methods [28], or when measurements are made over a large range of flow rates [12]. We follow the method, as used in ref [9], of choosing a value of C to match the number of fringes along the centreline.

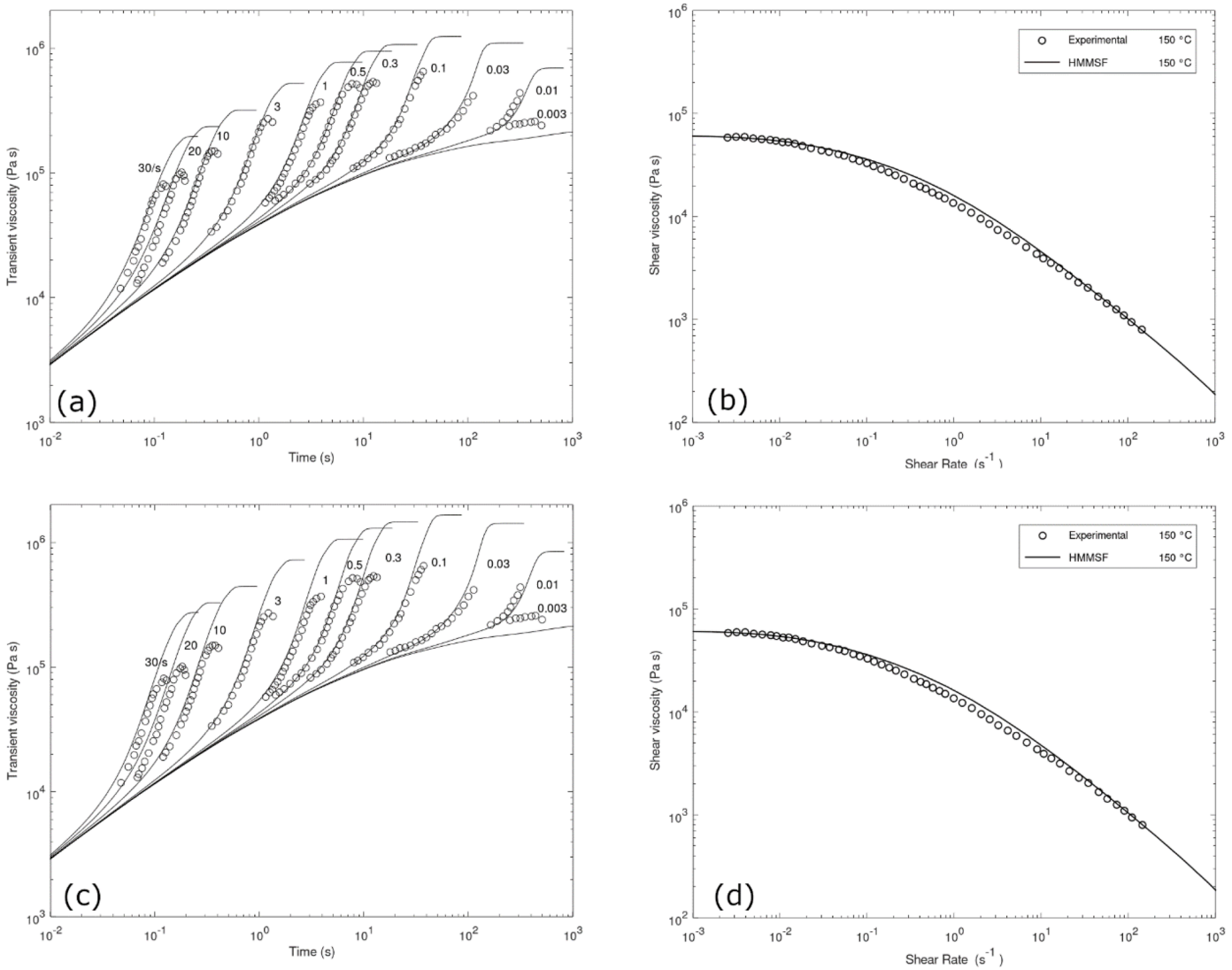

Fig. 7. Transient uniaxial extension and steady-state shear viscosity using $G_D = 2 \times 10^4$ *Pa* with β=0.09 ((a) and (b)), and with $G_D = 4 \times 10^4$ *Pa* with β=0.13 ((c) and (d)), compared with experimental uniaxial measurements (from [21]) and shear measurements (from [22]).

Fig. 6 compares experimental birefringence patterns, and the reconstructed birefringence from simulation stresses using the HMMSF model. At each value of flow rate the initial phase angle, θ, was adjusted such that the first clear fringe aligned with experiment, then a value of the Stress Optical Coefficient, C, was found such that the number of fringes along the centreline matched. The values of C that were obtained varied from $1.37 \times 10^{-9}\ m^2/N$ at the lowest flow rate to $1.11 \times 10^{-9}\ m^2/N$ at the highest flow rate, showing variation by a factor of 1.23 over this range. The variation in the apparent optical stress coefficient is considered later in this work. There is very good comparison at each flow rate for the overall 'bow' shape in the converging flow, and also its width. Peak stresses occur near the 'lip' of the die for both experiment and simulation, and the number of birefringence fringes in this feature match very accurately, showing a close match of stress levels in this complex region using the HMMSF model. Stress relaxation is clearly visible along the centreline, downstream of the lip, in both experiment and simulation; the close correspondence of fringe position shows a good quantitative match between the two. Comparison of these HMMSF results with the results given for the MSF-CCR model in ref [9] show considerable improvement overall, notably in terms of the overall shape of the inlet 'bows', as well as the correspondence of peaks around the 'lip'. In so far as the vortex size might be judged from birefringence patterns, vortex size and opening angle also appear better matched. The use of fully-developed inlet boundary conditions is responsible for some of the improvement in matching in the low stress areas (such as improving the match to the width of the 'bows') however high stress areas, such as the 'lip' peaks are little affected by the change to fully developed inlet boundary conditions, so these improvements are clearly due to the HMMSF model. The only significant qualitative difference between the experimental and simulation results lies in the region downstream of the lip peaks, where the 'stress fangs' (the areas that appear to be convected high stresses from the areas near the lip) are more pronounced in experimental results than in simulation results. This is examined in more detail later in this work.

5. Results with larger values of the dilution modulus, G_D

The dilution modulus parameter, G_D, was chosen as 7.0×10^3 *Pa* as this was consistent with the 'lower bound' that the measured rheological data showed. As clear 'necking' was seen during the extensional rheological measurements it is entirely possible that the true level of strain hardening of the material lies above the point indicated by $G_D = 7.0 \times 10^3$ *Pa*. We now investigate behaviour at significantly higher levels of strain hardening, using $G_D = 2 \times 10^4$ *Pa* and $G_D = 4 \times 10^4$ *Pa*. For each

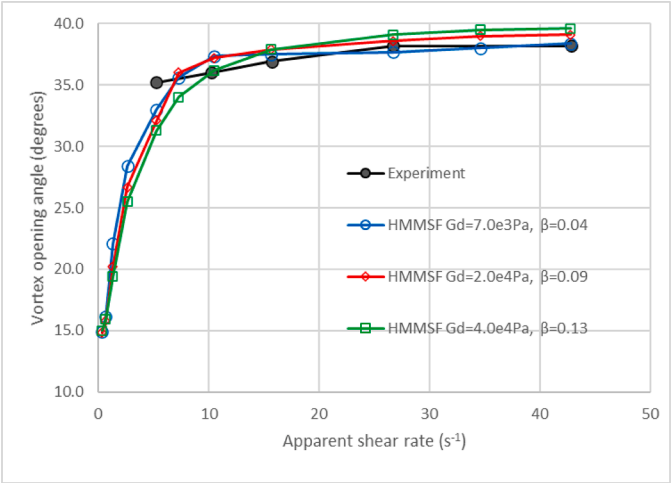

Fig. 8. Comparison between experimental results and simulation results using the HMMSF model with three different sets of (G_D, β) parameters.

of these values a value of β was found to match the rheological shear data; the corresponding values were found to be β=0.09 and β=0.13, respectively. The comparisons to uniaxial extensional data and shear data are shown in Fig. 7 for both of these higher values of G_D.

In Fig. 7, the uniaxial extensional viscosities with increased values of G_D (sub-plots (a) and (c)) generally rise well above the maximum values recorded in the experimental rheological measurements. This seems plausible as the maximum stresses recorded experimentally are reported to correspond to 'necking'. The rise-rates are also higher than with $G_D = 7.0 \times 10^3 Pa$ (see Fig. 2), and fit the data slightly less well at most extension rates in both sub-plots (a) and (c). The fit to shear data shows a greater rise above the experimental data in sub-plots (b) and (d). This evidence, so far, tends to give a slight preference towards the lower value of G_D.

Fig. 8 compares the HMMSF model, using all three values of G_D against the experimental data. The simulation curves follow a similar path, with some tendency for the higher values of G_D to rise less quickly towards the 'plateau' level (all 3 sets of simulations give a monotonically rising opening angle with apparent shear rate). There is a slight tendency for the opening angles at high rates to increase using the higher values of G_D (with β adjusted to match shear viscosity, accordingly), with an approximately 2° higher opening angle for $G_D = 4.0 \times 10^4 Pa$ compared to $G_D = 7.0 \times 10^3 Pa$. All 3 sets of parameters fit the opening angle data well, in comparison to the best previously published results using the MSF-CCR model.

Fig. 9 compares the computed birefringence patterns obtained using the highest value of G_D studied, $G_D = 4.0 \times 10^4 Pa$ (with β=0.13), with the experimental birefringence patterns obtained at the same flow rates. Values of the stress optical coefficient were obtained independently, using the same approach as used for $G_D = 7.0 \times 10^3 Pa$. The overall shapes of the patterns are similar to those obtained earlier, but with some detail differences. The patterns using $G_D = 4.0 \times 10^4 Pa$ show a greater tendency towards exhibiting 'stress fangs' at the higher rates, in keeping with this feature in the experimental data. Less favourably, the contours near the 'lip' of the contraction correlate fractionally less well in this region to those seen experimentally, than those in simulation using $G_D = 7.0 \times 10^3 Pa$. Perhaps the most significant feature shown by Fig. 9 is that a factor of 6 rise in G_D gives only a small difference in predicted stress birefringence patterns, when the rise in G_D is accompanied by an increase in β to maintain a match to shear viscosity data.

The values of the Stress Optical Coefficient, C, that were obtained at the two extreme values of G_D are plotted in Fig. 10. The values showed a steady reduction with apparent shear rate for both values of G_D. For $G_D = 7.0 \times 10^3 Pa$ the values drop from $1.37 \times 10^{-9}\ m^2/N$ at the lowest flow rate to $1.11 \times 10^{-9}\ m^2/N$ at the highest flow rate; a factor of 1.23 over this range. For $G_D = 4.0 \times 10^4 Pa$ the corresponding factor is 1.33. The value for $G_D = 7.0 \times 10^3 Pa$ is lower than for the MSF-CCR, which gave corresponding factors of 1.32 and 1.42 for two variants (see [9]), or the Double Convected Pom-Pom (DCPP) model which gave a factor of approximately 2.29 variation in apparent Stress Optical Coefficient over a factor of 10 change in apparent shear rates [12]. For context, a less developed viscoelastic model, the Upper Convected Maxwell model, varied by a factor of approximately 70 in apparent Stress Optical Coefficient over a factor of 10 change in apparent shear rate [12].

5.1. *Detailed study of birefringence order downstream of the slit*

The experimental results show clear 'stress fangs' downstream of the peak stress area near the lip of the contraction, which are largely absent from the simulated birefringence patterns. To resolve this difference more quantitatively, the positions of experimental and simulated fringes are plotted in detail at one flow rate (73.7 g/min) in this area. The positions of fringes were determined along lines at several distances from the centreline, and parallel to it; this was performed for both the experimental birefringence image and the simulated birefringence image. The line labelled "0%" is a line exactly along the centreline, the line labelled "30%" is a line at 30% of the distance from the centreline to the wall and so "90%" is a line very close to the wall. Fig. 11 shows the results for a rate of 73.7 g/min using $G_D = 7.0 \times 10^3 Pa$ and β=0.04 (the source image is shown in Fig. 6).

Fig. 11 shows that the experimental and simulated fringe orders along the 0%, 30% and 60% lines match very closely at this rate and parameter settings. The match at 60% is interesting as this line passes (very approximately) through the centre of the 'stress fang'. The close match shows that the difference in appearance between the measured and computed birefringence images is not caused by the simulation relaxing stress more quickly. The lines for 90% show the cause of the difference in appearance – the experimental birefringence orders drop much more quickly than those from the simulation, and this rapid drop appears to be the actual cause of the visual 'stress fangs'.

Fig. 12 shows the same comparisons, but for simulation results using $G_D = 4.0 \times 10^4 Pa$ and β=0.13 (as shown full field in Fig. 9). The comparisons along the 0%, 30% and 60% lines are less close than those using $G_D = 7.0 \times 10^3 Pa$ (a tendency found for many other comparisons between the two parameter sets within the paper). The same overall trend is seen however, with significantly better matches at 0%, 30% and 60% than at 90%. The simulation fringe orders on the 90% line drop slightly faster than with $G_D = 7.0 \times 10^3 Pa$ and β=0.04, giving a slightly stronger suggestion of 'stress fangs' as seen in Fig. 9. The larger value of β seems the probable cause of the faster drop in stress under shear, but there remains a marked difference between measured and simulated fringes along the line near the wall.

For both parameter sets, the measured drop rate in fringe order at 90% distance from the centreline appears very large in comparison to drop rates seen at other distances from the centreline, and also in comparison to the drop rate of the simulation at this distance. Clearly, shear rates near the wall will be higher than at other distances from the centreline and this suggests the possibility that the model isn't responding in the same way as the polymer to stretch followed by high shear. It is also worth recalling that the stress optical law is regarded as "semi-empirical" as it makes assumptions to link stress and birefringence [12]. Significant exceptions to the stress optical law have previously been demonstrated for high strains in elongational stretch [29, 30]. Polymer flowing near the 90% line will have had a history of significant stretch followed by high shear, and it is possible that the assumptions the stress optical law makes do not hold linearly in that flow regime.

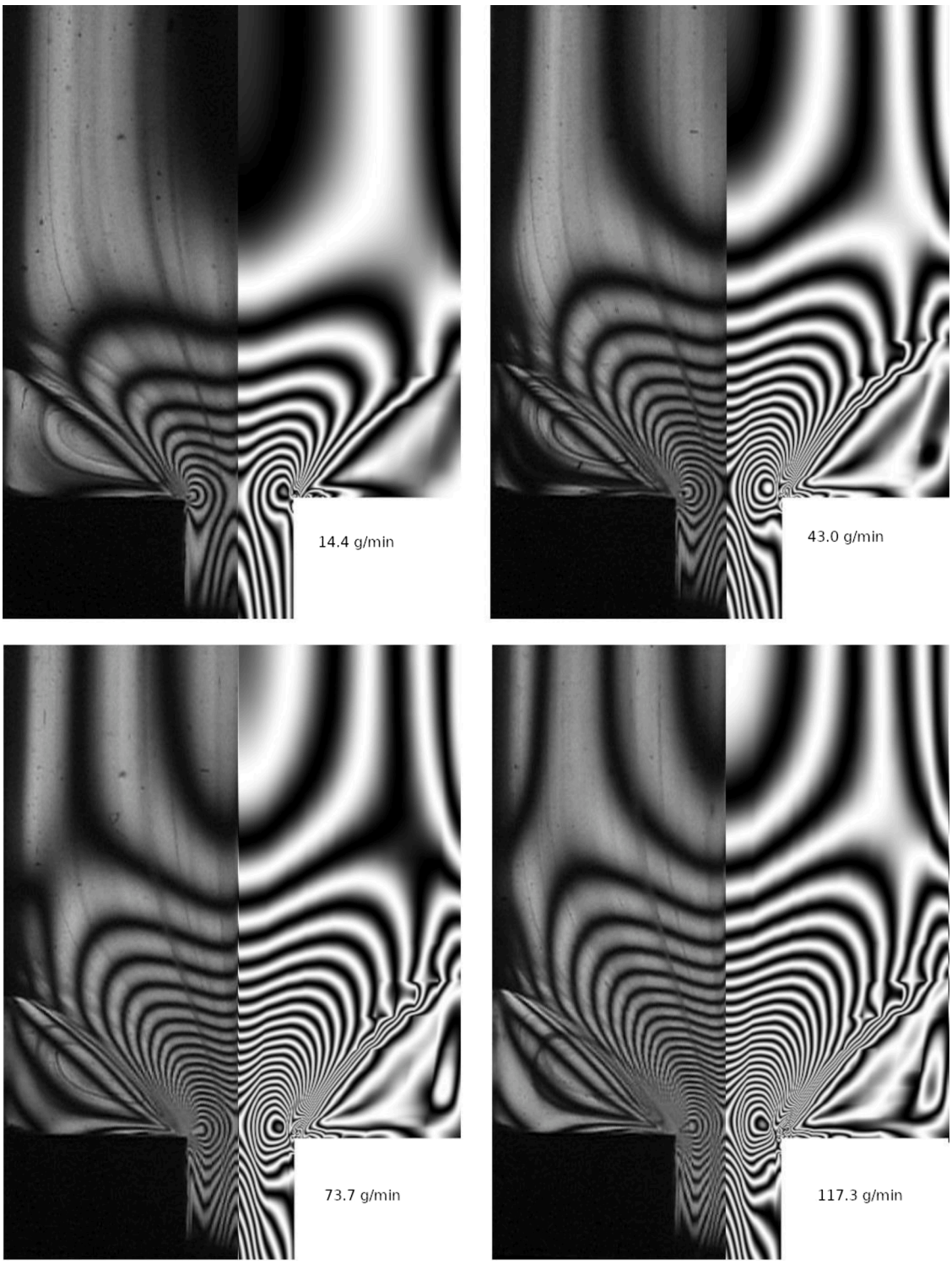

Fig. 9. Comparison between experimental birefringence measurements (left) and computed birefringence resulting from simulation using the HMMSF model (right), using G_D=4.0 $\times 10^4 Pa$ and β=0.13.

5.2. Parametric study of the effects of G_D and β on opening angles

The opening angles shown in Fig. 8 used different values of G_D, with β values chosen to match the rheological shear data. It is interesting to gauge the effects of parameters without this matching using the β parameter. Simulations were performed at 73.7 g/min, centred on G_D = 2.0 $\times 10^4 Pa$ and β=0.09. Two further simulations were performed at G_D = 7.0 $\times 10^3 Pa$ and G_D = 4.0 $\times 10^4 Pa$, while keeping β fixed at 0.09. Additionally two further simulations were performed at β=0.04 and β=0.13 while keeping G_D fixed at 2.0 $\times 10^4 Pa$. The results are shown in Fig. 13.

The point at the centre of Fig. 13 (G_D = 2 $\times 10^4 Pa$, β = 0.09) is a point that accurately fits the rheological data. The dashed line shows G_D being varied (keeping β fixed), and the dotted line shows β being varied, keeping G_D fixed. The ranges used for G_D and β are from the highest and lowest values used in earlier fits to rheological data. It can be gauged

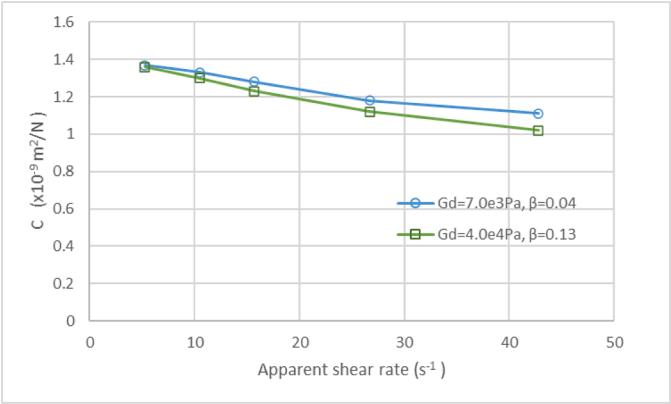

Fig. 10. Apparent (best fit) values of the stress optical coefficient, obtained at different apparent shear rates, for the parameter sets (G_D=7.0 × 10^3*Pa*, β=0.04) and (G_D=4.0 × 10^4*Pa*, β=0.13).

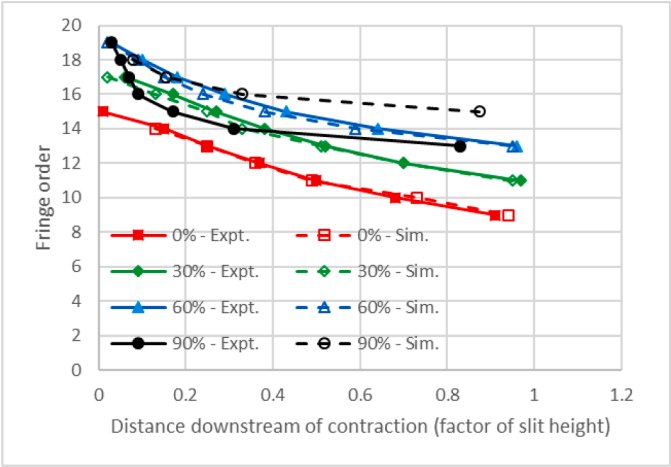

Fig. 11. Fringe order versus distance downstream of the slit opening (using G_D = 7.0 × 10^3*Pa* and β=0.04) at a rate of 73.7 g/min.

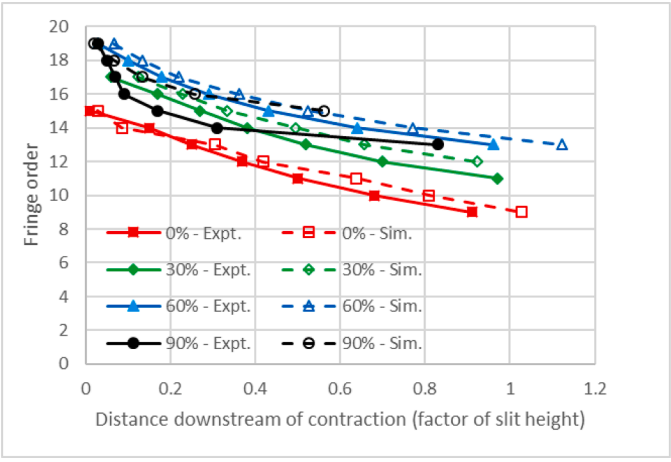

Fig 12. Fringe order versus distance downstream of the slit opening (using G_D = 4.0 × 10^4*Pa* and β=0.13) at a rate of 73.7 g/min.

from the diagram that a unilateral factor of 2 increase in G_D around this range gives an increase of approximately 3° in opening angle, while a factor of 2 increase in β reduces the opening angle by approximately 3°.

The effects of varying G_D on extensional viscosity are unchanged from those shown in Figs. 2 and 7 (since extensional viscosity predictions are unaffected by β). The effects on predicted shear viscosity can be seen in Fig. 14, where G_D is fixed at the central value of 2.0 × 10^4 *Pa*, while β is used at 0.04, 0.09 and 0.13.

The difference for these 3 values of β at the fixed value of G_D are fairly slight, requiring the detailed view (inset) to discriminate between them clearly. By contrast the same unilateral variation of β at a value of G_D = 2.0 × 10^4 *Pa* gives a more significant variation of over 6° in opening angle, as can be seen in Fig. 13.

6. Mesh convergence

In order to establish the mesh convergence of the method and the results, simulations were conducted on meshes of different densities at two rates (14.4 g/min and 73.7 g/min) and using two different parameter sets (G_D = 7.0 × 10^3 *Pa* with β = 0.04, and G_D = 4.0 × 10^4 *Pa* with β = 0.13). Three new meshes were used: Mesh-0.6, Mesh-0.8 and Mesh-1.2.

The meshes were produced by taking the mesh used for all work to this point (Mesh-1.0) and multiplying the number of elements along each structured mesh boundary by the factor included in the name of the new mesh. So, for example, Mesh-0.6 has 0.6 times as many elements in each direction (to nearest integer) as the original mesh, and so has the order of $(0.6)^3$ times as many elements in total. Hence there are two coarser meshes than the main mesh (Mesh-1.0), and one finer mesh.

The numbers of elements and nodes in each mesh are given in Table 3.

The variation of opening angle is shown in Fig. 15 for the meshes. The variation is shown for two different flow rates and for the two different parameter sets. The coarsest mesh (with 536 elements) gives opening angles that are approximately 1.5° to 2° below the other three meshes, however the opening angles are seen to be quite settled for the three finest meshes, with a maximum variation of 0.2° between these three. The opening angles appear to be well determined by the mesh density of Mesh-1.0 (at 1746 elements). The variation of 0.2° that is suggested (from comparison of the three finest meshes) is slight to the graphical scales of Figs. 5 and 8.

Fig. 16 compares the birefringence patterns produced using results from the main mesh (Mesh-1.0) and the finest mesh (Mesh-1.2). The flow rate in each case is 73.7 g/min, and the parameters used are G_D = 7.0 × 10^3 *Pa* and β = 0.04. Both birefringence images use the same value of stress optical coefficient that was used in Fig. 6 (1.18 × $10^{-9}m^2/N$, at 73.7 g/min). The differences are seen to be slight with a close match of the peak near the lip, and close correspondence along the centreline upstream of the lip. The greatest difference is seen on the centreline downstream of the lip, where the stress falls slightly less quickly with the finer mesh; this seems likely to be due to a slightly modified flow profile due to resolving this narrow section more closely. The difference can be judged from Fig. 16 to be a small fraction of a fringe separation, and so would only slightly affect the detailed results shown in Fig. 11.

In summary, the convergence study shows that the simulation method gives convergence with mesh refinement for both vortex opening angles and birefringence, and the results produced by the main mesh (Mesh-1.0) differ only in fine detail from those produced by a second finer mesh.

7. Discussion and conclusions

The HMMSF model gives an exceptionally accurate fit to the uniaxial extensional data for Lupolen1840H using the parameter G_D set to 7 × 10^3 *Pa*. This is particularly noticeable in the close match to rise rates over an extension rate from 0.01s^{-1} to 30s^{-1}. It is noticeably closer than the previous best fit of which we are aware, using the MSF-CCR model [9] The fit to the available rheological shear viscosity data is also very

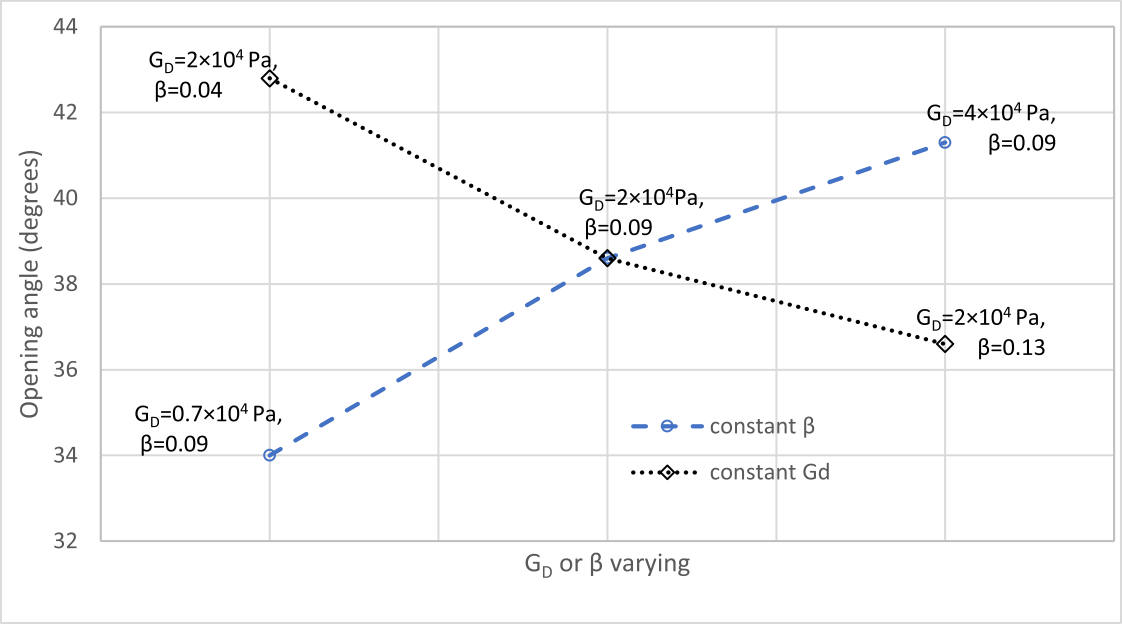

Fig. 13. Sensitivity of opening angle to varying G_D with constant β, and varying β with constant G_D.

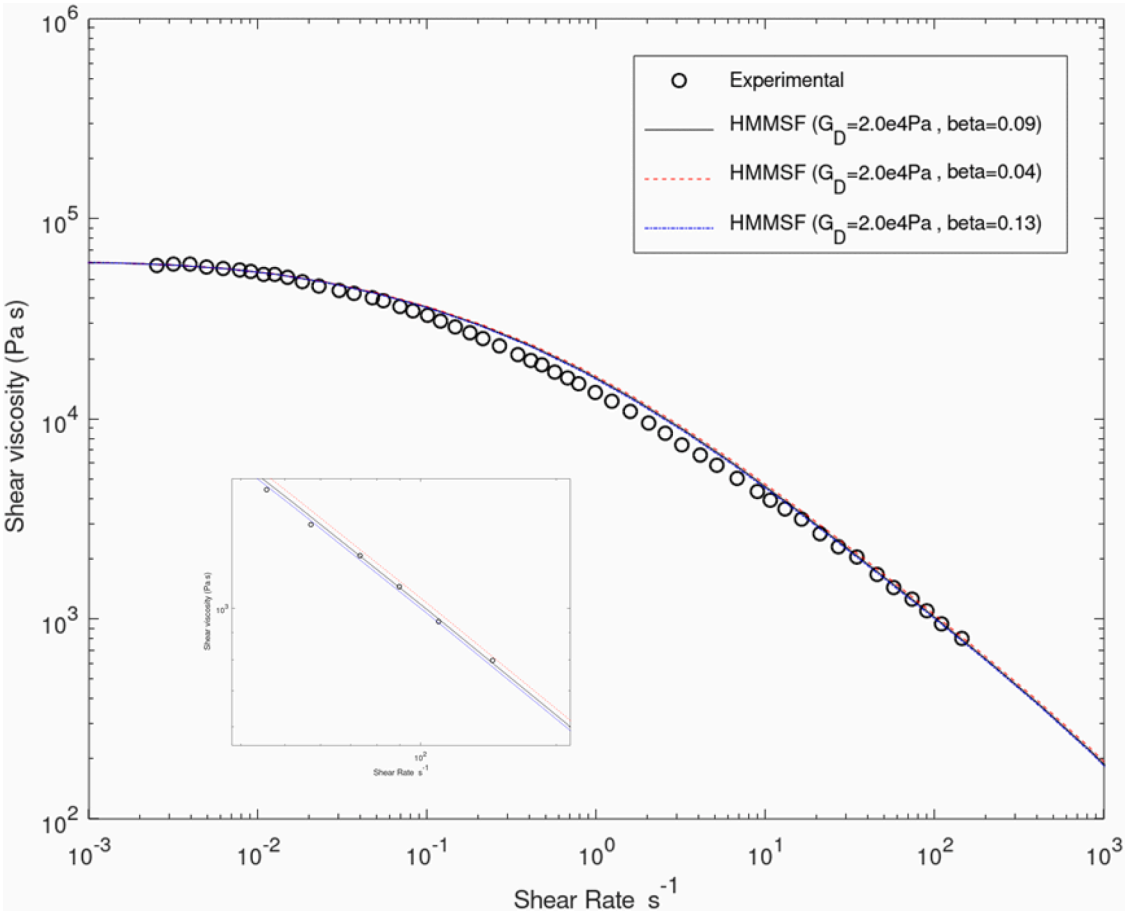

Fig. 14. Comparison of steady-state measured data with HMMSF using G_D=2.0 $\times 10^4 Pa$ and three different values of β (0.04, 0.09 and 0.13). Inset shows detail around $10^2\ s^{-1}$.

good, although there is a slight overprediction at 'mid-range' values around $1s^{-1}$. The HMMSF model has previously been shown to accurately fit transient shear viscosity data, and uniaxial, planar and equibiaxial extensional data for a large range of polymers including several LDPEs and HDPEs, so this overprediction against one data set may not be significant.

Table 3
Element and node numbers in meshes used in assessing mesh dependence.

Mesh name	Number of elements	Number of nodes
Mesh-0.6	536	5499
Mesh-0.8	990	9537
Mesh-1.0	1746	16,315
Mesh-1.2	2814	25,725

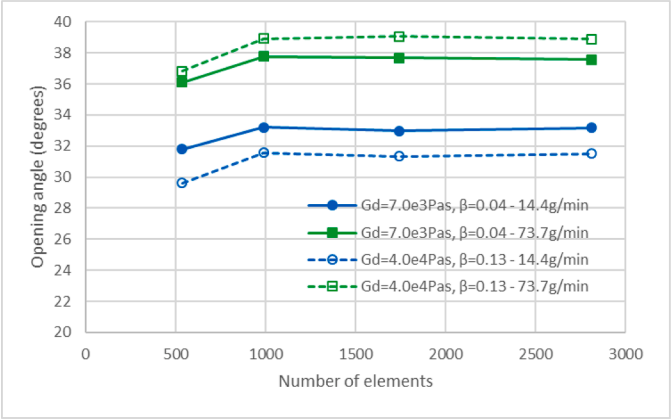

Fig. 15. Variation of simulated opening angles with mesh density for two flow rates and two parameter sets.

Fig. 16. Simulated birefringence patterns using the main mesh (Mesh-1.0) and the finer mesh (Mesh-1.2). Both are produced with a stress optical coefficient of $1.18 \times 10^{-9} m^2/N$.

Adaptation of existing MSF-CCR code to simulate the HMMSF presented no particular difficulties, although careful attention was needed on the size of time steps used in calculating the modal molecular stress functions, $f_i(t,t')$, as described in the text. The 'mirroring' method to give a fully developed inlet profile added realism to the simulation, and also improved the quality of match between simulated and observed birefringence pattern very significantly, particularly in the low stress areas near the inlet. Fully developed inlet boundary conditions also had an effect on vortex opening angles, general causing a reduction of 1 or 2° in comparison to a parabolic inlet profile of the same overall flow rate.

The conspicuous achievement of the model, from a flow simulation perspective, is the excellent quantitative match to both the level of vortex opening angles, and also to matching the 'plateau-like' form of the opening angles, as exhibited by the polymer experimentally. This can be contrasted with the more gradual rise exhibited by the MSF-CCR (as shown in Fig. 5), which is the closest previous simulation of this polymer of which we are aware. Further, we are not aware of previous 3D simulations of any specific polymer giving a comparable close match to experimental vortex opening angle over a large range of flow rates.

The match between experimental and predicted stress birefringence pattern is also very good, and slightly better in terms of the overall form of the 'butterfly' patterns towards the contraction in comparison to the results from the MSF-CCR [9]; a significant part of this improvement can be attributed to the use of fully-developed inlet boundary conditions. An apparent stress optical coefficient was found for each flow rate to match the number of fringes along the centreline. Using only this, the number of fringes around the lip was found to agree closely with experiment when using a value of the parameter G_D set to 7×10^3 *Pa*. The variation of apparent stress optical coefficient is of interest as, for $G_D = 7 \times 10^3$ *Pa*, it varied by a factor of 1.23 over a factor of 8 change in flow rate. There are few papers where the variation of apparent stress optical coefficient has been studied explicitly, however the current value is significantly lower than other values – 1.32 and 1.42 for two variants of the MSF-CCR over the same range [9], a factor of 2.29 over a factor of 10 range of flow rates for the Double Convected Pom-Pom (DCPP) model [12], and a factor of 70 change over that same range for the (less developed) Upper Convected Maxwell Model [12].

The experimental uniaxial extensional data can be viewed as a 'lower bound' on the strain hardening behaviour of Lupolen 1840H, especially as 'necking' was observed. The value of $G_D = 7 \times 10^3$ *Pa* corresponds to this lower bound. Higher values of G_D were used to give stronger strain hardening, whilst the parameter β was increased to maintain a fit to the experimental shear viscosity data. Despite quite large increases in G_D (a factor of approximately 6), the vortex opening angles and birefringence patterns change quite slightly when the parameter β was adjusted to maintain a fit to shear data. However, there are a number of comparisons in this work where using $G_D = 7 \times 10^3$ *Pa* gives a better match to experiments than those obtained using higher values of G_D (2×10^4 *Pa* or 4×10^4 *Pa*). These factors are: a better fit to the rate of strain hardening in uniaxial extension, a better fit to steady-state shear viscosity, a better match to experimental vortex opening angles and a lower variation in apparent stress optical coefficient over the range of flow rates studied. In view of these factors a value of $G_D = 7 \times 10^3$ *Pa* can be considered to give the best results for this polymer. It is remarkable, however, that when G_D is altered so much (while modifying β to maintain a match to steady-state shear viscosity data) the opening angles and stress birefringence actually vary so little from the experimental measurements.

The salient difference between experimental and simulated birefringence patterns was the much less pronounced 'stress fang' in the simulated results. Detailed study showed that the visual effect is primarily caused by rapidly falling fringe order near the wall, around the lip of the contraction; this rapid fall of fringe order is much less pronounced in the simulation. The suggestion is that the difference arises because some aspect of polymer flow is not captured by the model. It is

also worth considering the possibility that the assumptions of the stress optical law may not hold in the particular flow regime near the downstream wall (significant stretch followed by high shear). See Refs. [12, 29, 30].

A 'unilateral' approach to changing a parameter was examined to see its effect (for example, changing G_D but leaving β unchanged). In this approach a close fit to the rheological shear viscosity measurement was not maintained, and there was a very marked variation in vortex opening angles.

The HMMSF constitutive model has already been shown to accurately fit a wide range of polymers (including HDPE, LDPE and LLDPE) in a wide range of viscometric measurements, including shear viscosity, first and second normal stress differences, and extensional viscosity in uniaxial, planar and biaxial extension [16, 17, 18]. In this work it has been used in the simulation of a 3D abrupt contraction flow, and shown to give an exceptionally good match to experimental vortex opening angles and stress birefringence for an LDPE melt. We are not aware of any comparable match between simulation and experiment for a contraction flow over a large range of flow rates, suggesting that the HMMSF model is a very significant step forward for quantitative simulation of polymer melt flows.

Declaration of Competing Interest

The authors declare that they have no known competing financial interests or personal relationships that could have appeared to influence the work reported in this paper.

Acknowledgements

The authors are grateful to Professors Manfred Wagner and Esmaeil Narimissa for invaluable correspondence and insights into the HMMSF model.

Appendix A. The effect of using fully-developed inlet boundary conditions on birefringence comparisons

Fully-developed inlet boundary conditions were used in this work, as described in Section 4. Fig. A.1 shows comparisons between the experimental and simulated birefringence patterns using parabolic inlet boundary conditions (as used in reference [9]), and using fully-developed boundary conditions as used in the current work. The flow rate is 73.7 g/min and the material parameters used were $G_D = 7.0 \times 10^3\ Pa$ with $\beta = 0.04$. A value of stress optical coefficient of $1.16 \times 10^{-9}\ m^2/N$ was found to match the peak centreline stress using parabolic inlet boundary conditions, which differs only slightly from the value found for the fully-developed inlet boundary conditions at this rate ($1.18 \times 10^{-9}\ m^2/N$). The match is notably better in the low-stress areas near the inlet using fully-developed boundary conditions, particularly when comparing the horizontal positions of the fringes. The fringes in the low stress inlet area are also sharper than with the parabolic inlet. We believe this improvement is due to the stress in these areas being computed by tracking back along fully-developed paths to a (matching) fully-developed inlet. Using parabolic inlet boundary conditions, on the other hand, means there will be an artificial transition from parabolic flow at the inlet to a more developed flow profile downstream, with a complex effect on the stress computation.

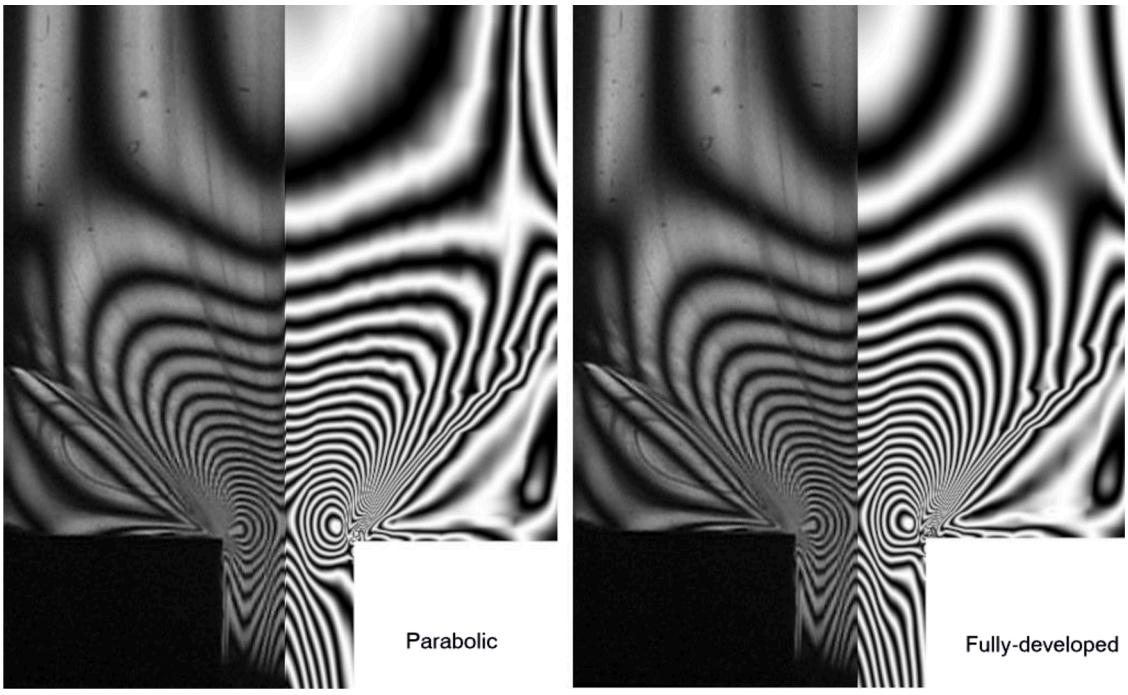

Fig. A.1. Comparisons between experimental and simulated birefringence using parabolic inlet boundary conditions (left comparison) and fully-developed inlet boundary conditions (right comparison).

References

[1] M.H. Wagner, A constitutive analysis of uniaxial elongational flow data of low-density polyethylene melt, J. Non-Newt. Fluid Mech. 4 (1978) 39.
[2] P. Olley, A study of the quadratic molecular stress function constitutive model in simulation, J. Non-Newtonian Fluid Mech. 125 (2005) 171.
[3] M.H. Wagner, J. Schaeffer, Assessment of nonlinear strain measures for extensional and shearing flows of polymer melts, J., Rheol. Acta 33 (1994) 506.
[4] M.H. Wagner, P. Rubio, H. Bastian, The molecular stress function model for polydisperse polymer melts with dissipative convective constraint release, J. Rheol 45 (2001) 1387.
[5] T.C.B. McLeish, R.G. Larson, Molecular constitutive equations for a class of branched polymers: the Pom–Pom polymer, J. Rheol. 42 (1998) 81.
[6] B. Robertson, R.L. Thompson, T.C.B. McLeish, I. Robinson, Polymer extrudate-swell: from monodisperse melts to polydispersity and flow-induced reduction in monomer friction, J. Rheol. 63 (2019) 319.
[7] G. Marrucci, Dynamics of entanglements: a nonlinear model consistent with the Cox–Merz rule, J. Non-Newtonian Fluid Mech. 62 (1996) 279.
[8] M.H. Wagner, H. Bastian, P. Hachmann, J. Meissner, S. Kurzbeck, H. Munstedt, F. Langouche, The strain-hardening behaviour of linear and long-chain branched polyolefin melts in extensional flows, Rheol. Acta 39 (2000) 97.
[9] P. Olley, T. Gough, R. Spares, P.D. Coates, An experimental and simulation comparison of a 3-D abrupt contraction flow using the molecular stress function constitutive model, Plastics, Rubber and Composites 50 (2021) 18.
[10] I. Sirakov, A. Ainser, M. Haouche, J. Guillet, Three-dimensional numerical simulation of viscoelastic contraction flows using the Pom–Pom differential constitutive model, J. Non-Newtonian Fluid Mech. 126 (2005) 163.
[11] R. Tenchev, T. Gough, O.G. Harlen, P.K. Jimack, M.A. Walkley, Three dimensional finite element analysis of the flow of polymer melts, J. Non-Newtonian Fluid Mech. 166 (2011) 307.
[12] N. Clemeur, R.P.G. Rutgers, B. Debbau, Numerical simulation of abrupt contraction flows using the Double Convected Pom–Pom model, J. Non-Newtonian Fluid Mech. 117 (2004) 193.
[13] G. Boukellal, A. Durin, R. Valette, J.-.F. Agassant, Evaluation of a tube-based constitutive equation using conventional and planar elongation flow optical rheometers, Rheol. Acta 50 (2011) 547.
[14] G. Marrucci, G. Iannirubertо, Flow-induced orientation and stretching of entangled polymers, Philos. Trans. R. Soc. Lond. Ser A Math. Phys. Sci. Eng. 361 (2003) 677.
[15] E. Narimissa, V.H. Rolón-Garrido, M.H. Wagner, A hierarchical multi-mode MSF model for long-chain branched polymer melts part I: elongational flow, Rheol. Acta 54 (2015) 779–791.
[16] E. Narimissa, M.H. Wagner, Review of the hierarchical multi-mode molecular stress function model for broadly distributed linear and LCB polymer melts, Polym. Eng. Sci. 59 (2019) 573.
[17] L. Poh, E. Narimissa, M.H. Wagner, Modelling of elongational flow of HDPE melts by hierarchical multi-mode molecular stress function model, Polymers 13 (2021) 3217.
[18] L. Poh, B. Li, W. Yu, E. Narimissa, M.H. Wagner;, Modeling of nonlinear extensional and shear rheology of low-viscosity polymer melts, Polym. Eng. Sci 61 (2021) 1077–1086.
[19] E. Narimissa, M.H. Wagner, Review on tube model based constitutive equations for polydisperse linear and longchain branched polymer melts, J. Rheol. 63 (2019) 361.
[20] S.M.F.D. Syed Mustapha, T.N. Phillips, A dynamic nonlinear regression method for the determination of the discrete relaxation spectrum, J. Phys. D: Appl. Phys. 33 (2000) 1.
[21] M. Sentmanat, B.N. Wang, G.H. McKinley, Measuring the transient extensional rheology of polyethylene melts using the SER universal testing platform, J. Rheol. 49 (2005) 585.
[22] M. Zatloukal, Differential viscoelastic constitutive equations for polymer melts in steady shear and elongational flows, J. Non-Newtonian Fluid Mech. 113 (2003) 209.
[23] P. Olley, M.H. Wagner, A modification of the convective constraint release mechanism in the molecular stress function model giving enhanced vortex growth, J. Non-Newtonian Fluid Mech. 135 (2006) 68.
[24] P.K. Currie, Constitutive equations for polymer melts predicted by the Doi–Edwards and Curtiss–Bird kinetic theory models, J. Non-Newtonian Fluid Mech. 11 (1982) 53.
[25] M. Viryayuthakorn, B. Caswell, Finite element simulation of viscoelastic flow, J. Non-Newtonian Fluid Mech. 6 (1980) 245.
[26] J.L. White, A. Kondo, Flow patterns in polyethylene and polystyrene melts during extrusion through a die entry region: measurement and interpretation, J. Non-Newtonian Fluid Mech. 3 (1978) 41.
[27] J. Meissner, J. Hostettler, A new elongational rheometer for polymer melts and other highly viscoelastic liquids, Rheol. Acta 33 (1994) 1.
[28] D.G. Kiriakidis, H.J. Park, E. Mitsoulis, B. Vergnes, J.-.F. Agassant, A study of stress distribution in contraction flows of an LLDPE melt, J. Non-Newtonian Fluid Mech. 47 (1993) 339.
[29] T. Sridhar, D.A. Nguyen, G.G. Fuller, Birefringence and stress growth in uniaxial extension of polymer solutions, J. Non-Newtonian Fluid Mech. 90 (2000) 299.
[30] C. Luap, M. Karlina, T. Schweizer, D.C. Venerus, Limit of validity of the stress-optical rule for polystyrene melts: influence of polydispersity, J. Non-Newtonian Fluid Mech. 138 (2006) 197.